RSC Advances

PAPER

View Article Online
View Journal | View Issue

Cite this: *RSC Adv.*, 2016, **6**, 60845

Fabrication of magnetite nanocrystals in alcohol/water mixed solvents: catalytic and colloid property evaluation†

Srividhya J. Iyengar,[a] Mathew Joy,[a] A. Peer Mohamed,[b] Swati Samanta,[c] Chandan Kumar Ghosh[d] and Swapankumar Ghosh*[a]

Received 30th April 2016
Accepted 8th June 2016

DOI: 10.1039/c6ra11225k

www.rsc.org/advances

In this work, Fe_3O_4 nanocrystals have been synthesized by homogeneous precipitation in different alcohol/water (1 : 1) solvent mixtures at two different temperatures to elucidate the role of the dielectric constant (ε) of the reaction medium. The effects of different solvents on the catalytic activity of precipitated NPs in carbon combustion were examined. HRTEM images, SAED and XRD confirmed that the nanocrystals are of pure fcc inverse spinel Fe_3O_4 phase with narrow size distribution, and the crystals are completely dispersible in water. The morphological features of the nanocrystals, such as their surface termination and shape of the Fe_3O_4 NPs, were analyzed by HR-TEM. As ε decreases, the crystal size decreases for mono-ol systems compared to ~13 nm size in water, whereas ethylene glycol/water yields finer ~8.2 nm crystals although it has the highest ε among the mono-/poly-ols. A soot combustion study demonstrates that the catalytic activity is mainly due to the available surface area along with the exposure of active crystallographic facets. A study of the colloids by light scattering shows that the alcohol mediated process produces 16 to 33 nm MNP clusters composed of 2 to 3 particles in highly stable aqueous magnetic fluids. The relatively high temperature process favors higher crystallinity and particle size with reduced colloidal stability in the aqueous phase. The nanocrystalline powders and the dispersed colloids have excellent potential applications in biotechnology and selective catalysis and also as ferrofluids.

Introduction

Magnetite (Fe_3O_4; ferrosoferric oxide) is a well known magnetic material with high saturation magnetization. Ferromagnetic spinels are converted to superparamagnetic particles by reducing the crystal size to the nanoscale.[1] Nanofabricated Fe_3O_4 exhibits unique and tunable fundamental size- and shape-dependent magnetic, optical, and other properties.[2,3] Magnetic materials are used in magneto-optical switches, sensors, modulators, optical circulators, and optical isolators[4] and as magnetic adsorbents for anionic dye removal from waste water.[5] Magnetic nanofluids or ferrofluids are colloidal dispersions of single domain magnetic nanoparticles (MNPs) in a base fluid; they form a class of smart materials whose flow properties are adjustable *via* an external magnetic field.[6] The interparticle interactions which contribute to the aqueous colloidal stability can be expressed as a form of extended Derjaguin–Landau–Verwey–Overbeek (DLVO) theory.[7] In order to realize NPs with high levels of colloidal stability, there are two approaches: (1) high electrostatic repulsions among NPs, and (2) steric stabilization introduced by proper surface ligands. Bare MNPs synthesized in water are prone to aggregation because of (1) van der Waals and magnetic dipole–dipole attractive interactions,[8] (2) less electrostatic repulsion between the nanoparticles, and (3) a tendency to reduce the high free energy associated with the huge surface area to volume ratio in small nanocrystals. These interactions result in precipitation when gravitational forces overcome the thermal motion of the NPs. Moreover, water-based magnetic fluids are unique for their complex stabilization mechanisms and structural coordination under different conditions, as opposed to magnetic fluids, which utilize organic polar carriers.[9] It is essential to control both the primary particle size and agglomerate size of magnetic particles to obtain an optimum product.[10] Stable aqueous ferrofluids have been successfully used in biomedical applications such as contrast agents for electromagnetic tomography (MRI)

[a]*Project Management Division, CSIR-Central Glass & Ceramics Research Institute, Kolkata-700032, India. E-mail: swapankumar.ghosh2@mail.dcu.ie; srividhyaji@gmail.com; Fax: +91 33 24730957; Tel: +91 33 23223546*

[b]*Functional Materials Section (MSTD), CSIR-National Institute for Interdisciplinary Science & Technology (NIIST), Trivandrum-695019, India*

[c]*Material Characterization & Instrumentation Division, CSIR-Central Glass & Ceramic Research Institute, Kolkata-700032, India*

[d]*School of Material Science & Nanotechnology, Jadavpur University, Kolkata-700032, India*

† Electronic supplementary information (ESI) available: Additional TEM, EDS, XRD, crystallinity index, FTIR, PCS data, concentration/temperature trend, zeta potential *vs.* pH on nanofluids. See DOI: 10.1039/c6ra11225k

and hydraulic fracture diagnostics for imaging the brain and central nervous system, drug/gene-delivery platforms, tissue engineering, magnetically controllable catheters, and biosensors.[2] Major attention has also been directed toward the development of MNPs as sustainable nanocatalysts for specific chemical transformations having both economic and environmental significance, such as deodorizing catalysts,[11] oxide catalysts in solid propellants,[12] catalysts for exhaust gases of internal combustion engines[13] and degradation of organic pollutants in waste water;[14] the MNPs can easily be separated from the reaction mixture by an external magnetic field.

Magnetite nanocrystals can easily be synthesized by aqueous precipitation methods,[2] although they have the disadvantage of agglomeration of fine particles, which imposes a major challenge to the realization of the full potential of nanocrystalline powders. In the precipitation process, low dielectric constant solvents, *e.g.* alcohols, can alter the nucleation kinetics, which results in a reduction of the size and distribution of the resulting particles.[15–17] Mono- or polyol alcohols in water–alcohol mixed solvent also act as surfactants and suppress the growth of nanocrystals during alkali precipitation of metal oxide nanocrystals.[18,19] Guo and Xiao reported that the crystallite size and the crystallinity of the particles decreased with increasing IPA addition in hydrothermal reactions.[20] Ghosh *et al.* demonstrated that the radius (r) of nanocrystals produced in a precipitation reaction decreases with decreasing ε of the alcohol–water mixed solvent[18,21] following eqn (1):

$$\frac{1}{r} = \frac{kT\rho}{2m\gamma}\ln C + \frac{\rho z_+ z_- e^2}{8\pi m\gamma\varepsilon\varepsilon_0(r_+ + r_-)} \quad (1)$$

where ε_0 is the permittivity in a vacuum, r_+ and r_- are the radii of the charged z_+ and z_- ions, respectively, and e represents the charge of an electron (1.602×10^{-19} C). The solubility can be modulated by varying the composition of the solvent mixture. The formation (precipitation) of particles is strongly dependent upon the supersaturation of the solute, following classical nucleation theory. Supersaturation can be achieved by lowering the temperature, solvent evaporation, pH change, chemical reactions, alteration in solvent composition, *etc.* and is defined as the ratio of solute concentration (C) and saturation concentration; m is the molecular weight of the solute and γ is the interfacial energy between the solute and solution phases.

The effect of solvent can change the particle morphology; this effect is especially pronounced at higher concentrations of Fe-precursors (>0.5 M).[22] Chowdhury *et al.* evaluated the effect of alcohol–water mixed solvents with alcohols such as butanol, propanol, ethanol and methanol on β-FeOOH nanorods under hydrothermal conditions.[22] Cheng *et al.* reported a morphology evolution from compact microsphere-like single crystals to mesoporous hollow nanospheres by a polyol process.[23] Zhang *et al.* synthesized 15 to 300 nm magnetite crystals with controllably variable morphologies, including nanospheres to nano-octahedra/nano-hexaprisms in ethylene glycol–water mixed solvent.[24] Wang *et al.* fabricated well-defined micrometer sized magnetite crystals with star-shaped hexapods, octahedrons, concave octahedrons, and octahedral frameworks in IPA–water by a solvothermal approach.[16] Magnetite NPs with controlled morphologies such as core–shell structures and 1-D nanochains have also been reported by thermal decomposition in nonaqueous solvents.[25–27] Estelrich *et al.* reported high molecular weight (2 to 10 kDa) PEG coated magnetite ferrofluids with dipole–cation binding between the ether group of PEG and the positively charged NP core with suspension stability over two years.[19] Metal oxides become charged by the adsorption of hydrogen (H^+) or hydroxyl ions (OH^-) in aqueous suspensions, while remaining neutral at a specific pH called the point of zero charge (PZC).[28] Particles tend to aggregate as the electric potential approaches zero, known as the isoelectric point (IEP), under neutral conditions when there is no repulsion between the particles. It is well-known that under different colloidal conditions with potentials of either >20 mV or <−20 mV, particles repel each other (disruption of particle aggregation). The stability of the nanofluids and the clustering can easily be predicted from the zeta potential measurements. To avoid undesirable errors from using mathematical equations or the Henry formula to relate electrophoretic mobility to the ζ (zeta) potential of NPs, the surface charges of suspended particles are reported in terms of the ζ-potential.[29] Although the precipitation of metal oxides, *e.g.*, TiO_2, ZrO_2, CeO_2, and SiO_2, in alcohol/water mixed solvents has already been reported,[7,15,21] there is no systematic study on the effect of solvents with variable dielectric constants and precipitation temperatures on magnetic nanocrystals; to the best of our knowledge, there is no study on the effect of solvents/precipitation temperatures on the catalytic and colloidal properties/stability of aqueous suspensions of magnetite NPs.

Herein, we report the effect of various alcohols with different polarities on the size, colloidal stability, reactivity, and other related properties of magnetite nanocrystals by ammonia precipitation. Six alcohols have been employed with decreasing ε value in the order of ethylene glycol (EG) > diethylene glycol (DEG) > ethanol (EA) > *n*-propanol (*n*PA) > isopropanol (IPA) > polyethylene glycol (PEG). Mixed solvents of 1 : 1 water–alcohol produced small Fe_3O_4 NPs in the size range of 8 to 13 nm. The powders as well as the nanofluids have been characterized thoroughly by various techniques. The crystal structure and magnetic properties of the resulting colloidal particles have been investigated by X-ray diffraction (XRD), transmission electron microscopy (TEM), thermal analysis (TG-DTA), and vibrating sample magnetometry (VSM). The hydrodynamic size as well as the zeta potential was evaluated by photon correlation spectroscopy (PCS). To evaluate the colloidal stability, extensive zeta potential measurements have been carried out. The catalytic activity of the crystals investigated by diesel soot combustion have been explained in terms of the texture coefficients of different crystal planes, sizes and BET surface areas. This study lays a strong foundation to relate this activity on a physical basis for future nanomaterial development.

Experimental

Materials

For the synthesis of pure and surface functionalized magnetite nanocrystals, the chemicals used, Fe(II) chloride (98%) and

Fe(III) chloride (97%), were supplied by Sigma Aldrich. Absolute EA (99.9%), and *n*PA (AR) were purchased from S.D. FINE-CHEM Ltd, India. EG (guaranteed reagent, GR), DEG (for synthesis), PEG-400, acetone (GR), IPA (GR), methanol (GR), and 25% ammonia were procured from Merck, India. The chemicals for the syntheses were used as received without any purification. All the syntheses, washings and dilutions were carried out with Millipore water with resistivity 18.2 MΩ cm@25 °C after purging with ultrapure nitrogen gas (99.999% purity) to remove dissolved oxygen from the water.

Preparation

To fabricate the magnetite nanocrystals, an 8.4 mmol portion of $FeCl_2 \cdot 4H_2O$ and 16.8 mmol $FeCl_3 \cdot 6H_2O$ (such that $Fe^{3+}/Fe^{2+} = 2$) were dissolved in 35 ml 1 : 1 water–alcohol mixed solvent deaerated by purging with nitrogen gas for 30 min in a 100 ml three-neck round bottom flask. Several alcohols, *ca.* EA, *n*PA, IPA, EG, DEG and PEG-400, were used in this study. The reaction mixture was heated to 80 °C with a hot-plate magnetic stirrer and was maintained at this temperature for ~30 min with continuous stirring and nitrogen purging in a closed setup. Subsequently, the reactor was cooled naturally to 40 °C and was kept constant at this temperature. About 15 ml NH_3 solution was added to the homogeneous mixture in one portion when the reaction mixture turned black (pH ~ 11). Vigorous stirring and the temperature (40 °C) were maintained for 30 more min; the mixture was then allowed to cool to ambient temperature. At this point, the net Fe^{2+} concentration was 168 mM. The settled black precipitate was subjected to repeated alternating magnetic decantation and washing with water to remove impurities; the final washing step was performed with methanol to break down hard agglomerates. The fine powder form of magnetite was obtained by drying the resulting black slurry in a vacuum oven at 60 °C and preserving it in a desiccator for further characterization; the samples are labeled with the corresponding alcohol abbreviations. Magnetite precipitated in water at 40 °C is designated as WA. The magnetite was also precipitated at 80 °C to study the effect of temperature and was labeled with the alcohol abbreviation followed by a number (the precipitation temperature), *e.g.*, EG80 stands for magnetite in ethylene glycol–water solvent at 80 °C.

Instrumental

Transmission electron microscopy, including selected area electron diffraction (SAED) analysis, was used to ascertain the particle shape, size and crystal structure of the synthesized materials using a FEI Tecnai 30 G^2 S-Twin high resolution HR-TEM operated at 300 kV. The TEM grids were prepared by drop-casting (~15 μl) the nanopowder dispersions onto 400 mesh amorphous-carbon coated copper grids and allowing the solvent to evaporate. The elemental composition of the materials was determined using an EDAX spectrometer (Fischione Instruments, Inc., USA). The crystalline phase and crystal dimensions of the material were determined from the powder XRD patterns recorded with a Bruker D8 Advanced diffractometer using CuKα_1 radiation ($\lambda = 1.5406$ Å) in the 10° to 80° 2θ range with a step size of 0.05° 2θ and a scan speed of 4° min^{-1}. The crystallite size of the powder materials was determined using the Debye–Scherrer expression,[18] given in eqn (2):

$$D_{XRD} = \frac{0.9\lambda}{\beta_{2\theta} \cos \theta} \quad (2)$$

Standard Harris analysis was performed on the X-ray data of the magnetite powders to estimate the preferred orientation of specific crystal planes and is expressed as the texture coefficient, $C(hkl)$.[2] Magnetic measurements of the powder specimens were made using VSM (Lakeshore 7305, US) at 300 K.

The specific surface area, pore volume and pore size distribution of the magnetite powders were determined from the N_2 adsorption data following the Brunauer–Emmett–Teller (BET) method at 77 K using Quantachrome NovaWin Instruments (version 10.01) after degassing the powders at 200 °C for 3 h. The particle size (D_{BET}) was also calculated from the BET surface area (S_{SA}) using equation with an assumption that all the particles are spherical and unclustered, where $\rho = 5.18$ g cm^{-3} for magnetite.[2]

The average particle size of the NP suspensions and the size distribution, charge and colloidal stability of the synthesized magnetite based aqueous nanofluids were determined by the light scattering technique using a Zetasizer Nano-ZS (Malvern Instruments, Malvern, UK). The instrument uses a 4 mW He–Ne laser ($\lambda = 632.6$ nm) to illuminate the sample and measures the time dependent fluctuation in the intensity of light scattered from particles in suspension at a fixed scattering angle of 173°. This technique measures the Brownian motion of the NPs in suspension and relates their correlation time to the particle size using the Stokes–Einstein equation:

$$D_{PCS} = \frac{kT}{3\pi\eta D} \quad (3)$$

where D_{PCS} is the hydrodynamic diameter of the NPs, k is Boltzmann's constant, T is the absolute temperature (K), η is the viscosity (mPa s) and D represents the translational diffusion coefficient (m^2 s^{-1}). About 10 mg of magnetite powder was dispersed in 10 ml Millipore water by subjecting it to ultrasonication for ~20 min. The size data and the polydispersity index (PDI) were obtained from the correlograms by the cumulant analysis method. A second-order cumulant analysis was performed. The hydrodynamic diameter (Z_{av}) was determined from the first cumulant and the PDI was determined from the second cumulant divided by the square of the first cumulant.[30] The surface charge was estimated by measuring the zeta potential converted from the electrophoretic mobility of the dispersion in water at 25 °C using the Smoluchowski formula using Malvern Zetasizer Software v. 7.11. In order to determine the PZC, the pH of the dispersion was adjusted either with aqueous 10^{-3} M NaOH or H_2SO_4. The pH of the well dispersed magnetite fluids was checked just before each ζ-potential measurement.

Thermogravimetry (TG) and differential thermal analysis (DTA) was used to investigate the thermal reactions in the synthesized nanocrystals using a Simultaneous Thermal

Analyzer (STA 449 C, NETZSCH, Perkin-Elmer, US) under ultrapure nitrogen purge. The heating ramp was 10 °C min^{-1} in the 50 to 1000 °C temperature range. The reactivity of magnetite NPs in catalysing the combustion of carbon was investigated by controlled combustion of a 4 mg mixture of Fe_3O_4 catalyst, carbon soot (collected by burning diesel), and α-alumina under dry air atmosphere. The measurements were carried out by applying a sample with a ramp of 10 °C min^{-1} in the 50 to 700 °C range. Standard α-alumina was used as a reference. The sample for soot oxidation was prepared by mixing and grinding carbon, powdered Fe_3O_4 and alumina (average particle size ~450 nm, Condea Chemie, Germany) in a weight ratio of 1 : 4 : 5 in an agate mortar. The inert alumina powder was added to prevent any thermal runaways.

Results and discussion

Magnetic nanocrystals were synthesized by the ammonia precipitation technique in different alcohol–water mixed solvents at 40 and 80 °C. All the as-synthesized iron oxide powders were typically black in color, indicating the formation of magnetite crystals as the dominant phase. Selected bright-field TEM images, size distribution histograms depicting the mean size and its distribution, and SAED patterns of some representative magnetite specimens prepared in water as well as different alcohol–water solvents are shown in Fig. 1. Magnetite formation follows a crystallization pathway involving nanometer-sized intermediate primary particles that fuse to form the crystalline iron oxide phase, which further grows to spheroidal particles ~10 nm in size as the reaction continues.[31]

Average sizes were determined from the inspection of multiple TEM images of 100 to 120 particles, and these data are presented in Table 1. Relatively large spheroidal particles of *ca.* ~12.6 ± 1.9 nm were produced in water (panel A). When the reaction medium was changed to mixed solvents with mono- or poly-ol alcohols with appreciably lower dielectric constants, more or less polyhedral shaped smaller particles with average sizes in the 8.28 to 10.4 nm range with solvents in the order EG < DEG < *n*PA ≈ IPA < PEG < EA < WA were obtained. In alcohol–water solvents, the electrostatic attraction between initially precipitated primary particles is relatively low due to the lower dielectric constant of the solution. The possibility that the primary particles will agglomerate and grow is thus drastically reduced. Therefore, monodisperse NPs with narrow size distribution can be easily obtained. In mixed solvents with poly-ols, *e.g.*, EG, DEG and PEG, no such trend was observed. Although the 1 : 1 EG–water mix has the highest dielectric constant (58.95) among the solvents used in this work, next to water, it produced the smallest particles, with average sizes of 8.28 ± 1.22 nm. This is probably due to the presence of di-ol functional groups in this alcohol. High molecular weight poly-ols, *e.g.*, PEG and DEG (please see Fig. S3 in the ESI†), with high binding affinities to primary NPs act as surfactants and hinder the growth of particles by steric effects. From the TEM micrographs, it is difficult to comment on the degree of agglomeration among the NPs synthesized from different alcohols. The standard deviation (σ) of the size was a minimum of ~1.3 nm for the NPs

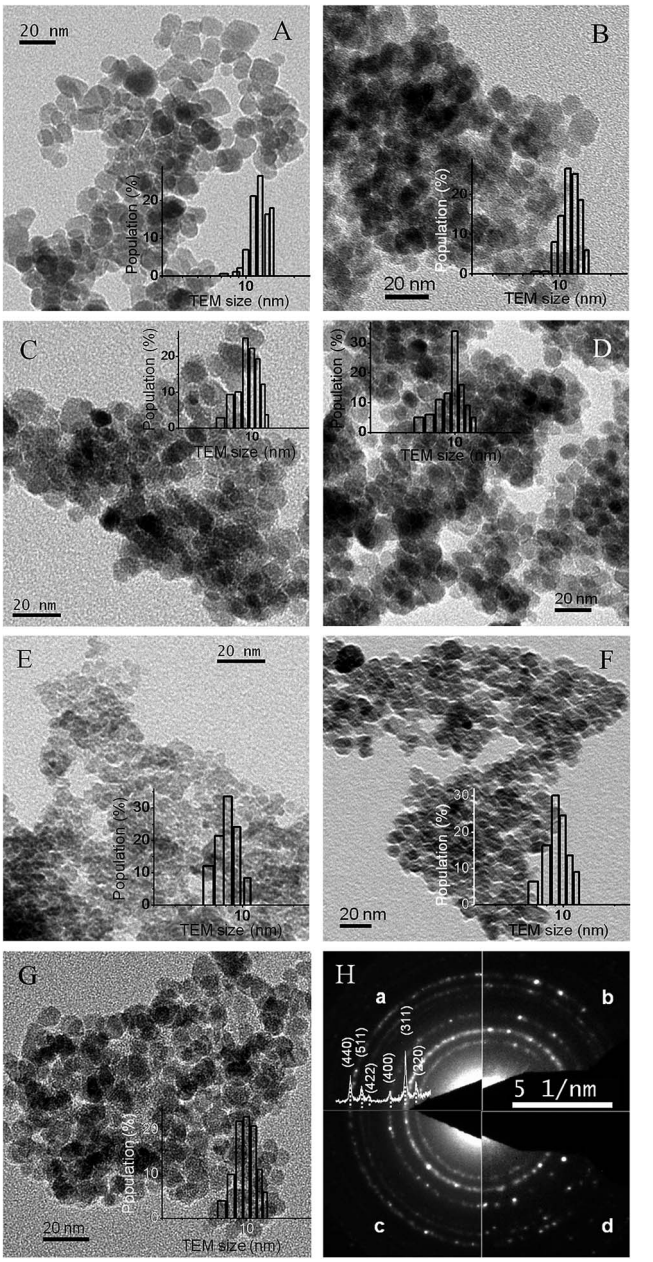

Fig. 1 TEM images of magnetite nanocrystals synthesized at 40 °C in (A) water and different mixed solvents with (B) EA, (C) *n*PA, (D) IPA (E) EG, (F) DEG and (G) PEG. The size distribution histograms of the corresponding nanocrystals for all the specimens are presented as insets to the TEM images. (H) SAED patterns of (a) DEG and its matching X-ray diffractogram with the (*hkl*) planes marked, (b) EG, (c) *n*PA, and (d) PEG.

from both EG (size 8.28 nm) and PEG (10.2 nm), followed by 1.53 nm in DEG (9.46 nm), whereas the σ values for the NPs from water (12.6 nm) and EA (10.26 nm) were 1.9 nm and 1.67 nm, respectively. Therefore, it is appropriate to conclude here that we are able to control the polydispersity by controlling the solvent characteristics. The size variation in the magnetite crystals synthesized in different solvents suggests the strong dependence of the crystal growth on the dielectric constant of the precipitating medium. The SAED patterns of DEG, EG, *n*PA, and PEG, given in Fig. 1H, show clear Debye–Scherrer rings for

Table 1 Physical size, crystallite size and surface areal size of magnetite synthesized from mixed solvents with different dielectric constants at different temperatures

Sample/ε (ref. 33)	D_{TEM}@40 °C (nm) ± SD	D_{XRD}@40 °C (nm)	D_{BET}@40 °C (nm)	D_{XRD}@80 °C (nm)
WA/80.2	12.6 ± 1.9	9.87	11.92	12.45
EA/52.4	10.26 ± 1.67	9.72	10.33	11.12
*n*PA/50.25	9.93 ± 1.45	9.69	13.71	11.86
IPA/50.05	10.03 ± 1.48	9.59	10.31	12.03
EG/58.95	8.28 ± 1.22	7.45	6.34	9.81
DEG/55.95	9.46 ± 1.53	8.31	8.96	10.69
PEG/46.3 (ref. 34)	10.2 ± 1.34	9.37	10.11	11.64

the (220), (311), (400), (422), (511) and (440) planes with corresponding interplanar spacings of 0.2967, 0.2532, 0.2099, 0.1715, 0.1616 and 0.1485 nm, respectively, matching the XRD pattern of DEG (JCPDS card no. 19-0629). In addition, the bright diffraction rings indicate that the NPs are well crystallized. The clustering observed in the TEM micrographs (Fig. 1) is attributed partly to drying artifacts on the TEM grid. The most important contributor to the formation of clusters is the interfacial and magnetic interactions among the NPs and the tendency to decrease the high surface free energy by clustering. The effect of the induction of surface hydration and the electric double layer over the MNP surface due to the mono/poly-ol mediated process on the state of clustering/growth of NPs is investigated by PCS in a later section.

Representative HR-TEM images of selected magnetite specimens with different projections are provided in Fig. 2. Fourier filtering was used to extract the lattice fringe information. The crystals resemble elongated hexagons (panel A), beveled cubes (2D) and two-dimensional projected contours.[32] Various projected shapes can result when the NP is viewed along different crystallographic directions.[32] Although the particles shown in Fig. 2 are different in shape, all of them are enclosed with three low-energy {100}, {110} and {111} surfaces. Careful examination of the HR images indicates that all the NPs are indeed single crystals; fringes belonging to predominant (111), (220), (311) and (400) planes with corresponding *d*-spacings of 0.4852, 0.2967, 0.2532 and 0.2099 nm could be identified. Point defects due to missing atoms or local deformation are observed on the nanocrystal surfaces in some instances; these are marked by arrowheads in Fig. 2C. The NPs have no apparent porosity, with well-defined crystalline structures. The NPs synthesized at 80 °C in respective media grew to larger sizes (see Fig. S1 in ESI†).

The elemental compositions of the Fe_3O_4 specimens were determined by EDAX. The peaks characteristic of O and Fe atoms were observed in the EDAX spectra, along with signals from C and Cu; the latter two belong to the carbon coated copper TEM grid (inset of Fig. S1 in the ESI†).

The X-ray profiles of the magnetic products synthesized from mixed solvents with different 'ε' values and temperatures and their calculated texture coefficients are shown in Fig. 3 and S2 of the ESI.† The diffraction patterns for all the powder samples show peaks for magnetite. The position and relative intensity of

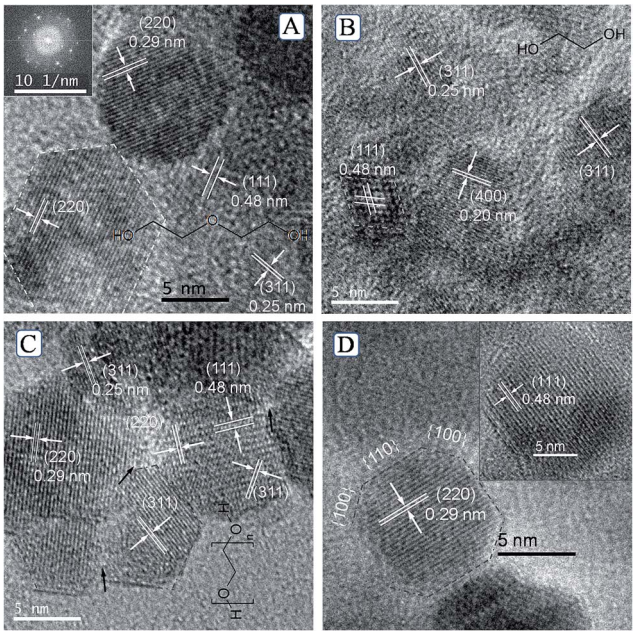

Fig. 2 HR-TEM images of magnetite nanocrystals fabricated in (A) DEG with its fast Fourier transform, (B) EG, (C) PEG, and (D) *n*PA (inset is another magnified crystal). The corresponding polyol structures are also shown as insets in their respective figures. Point defects in the nanocrystals are marked with black arrowheads in (C).

all diffraction peaks matched well with the characteristic fingerprint reflections of standard Fe_3O_4 with cubic fluorite structure (JCPDS 19-0629) having the space group $Fd\bar{3}m$ (227). The crystallite size was estimated using the width of the (311) reflection, employing the Debye–Scherrer equation (eqn (2)). The crystal sizes are in the 7 to 10 nm range, and the results are shown in Table 1. The X-ray peaks in the EG/water system are much broader than those in the other solvents. This is obviously because the smallest particles are produced in the EG/water system. In many cases, $D_{XRD} < D_{TEM}$, as D_{XRD} calculated employing the Scherrer equation ignores the broadening of the diffraction peaks due to microstrain in the lattice. X-ray often disregards the amorphous layer on the magnetite NP surface.[2]

The crystallinity indices (CI), as obtained from the XRD patterns of the nanocrystals precipitated at 40 and 80 °C, are in the ~78 to 95% range, indicating reasonably high crystallinity (Table S1†). The CI for WA is 91%; it decreased to ~79% in EG and increased to 95% in the same solvent when the precipitation temperature was increased to 80 °C (Table S1†). The average crystallite size grows and the crystallinity improves with increasing reaction temperature in spite of the decrease in ε of the reaction medium at higher temperatures.

Standard Harris analysis of the XRD patterns confirmed that the nanocrystals synthesized from alcohol media have proportionately higher active crystal facets compared to the nanocrystals synthesized from pure aqueous media. The texture coefficient data indicates that aqueous media produced magnetite crystals with minimum exposed active (220) facets. Preferentially grown active {110} and {100} planes with texture coefficient values in the range of 1.1 to 1.3 were obtained in all

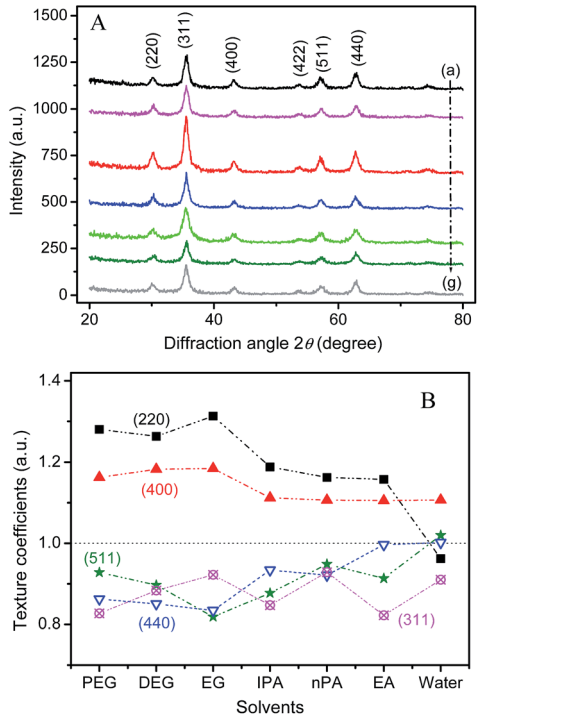

Fig. 3 (A) XRD patterns of magnetite crystals (a) WA, (b) EA, (c) *n*PA, (d) IPA, (e) EG, (f) DEG, (g) PEG, and (B) calculated texture coefficients.

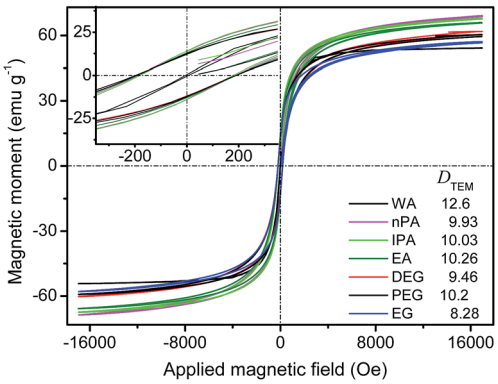

Fig. 4 Room temperature magnetization studies on the magnetite powders synthesized at 40 °C as a function magnetic field (up to 1.7 Tesla). Inset (left top) shows the respective zoomed hysteresis curves.

Table 2 Detailed VSM analysis of magnetite at 300 K

Sample/ε	M_S (emu g^{-1})	M_R (emu g^{-1})	H_C (Oe)
Bulk	84		115–150
WA/80.2	57.1	0.74	3.95
EA/52.4	65.82	13.0	188.2
*n*PA/50.25	68.79	14.1	187.2
IPA/50.05	67.62	14.2	180.3
DEG/55.95	61.89	12.4	195.5
PEG/46.3	60.33	12.5	197.2
EG/58.95	57.12	12.2	191.5

the alcohol solvents, with the highest being ~1.3 in EG, DEG and PEG, by inhibiting the growth of the (311) and (511) crystal facets. We now note that aqueous precipitated magnetite in the presence of PEG shows well developed and predominant {100} surfaces (T_C 1.163), as reported earlier.[32] Hence, this study opens a 'conceptual' possibility of producing nanocrystals in alcohol–water medium with predominant active facets, which may improve the physicochemical properties of the material and allow superior performance.

Fe_3O_4 nanocrystals are 'soft' magnetic materials in the sense that they quickly switch magnetization direction once the external magnetic field is reversed. This fact is experimentally shown using VSM in Fig. 4. It is evident that all the specimens showed ferromagnetic behavior at room temperature (~300 K), with the hysteresis loops showing saturation magnetization (M_S), remanent magnetization (M_R) and coercivity (H_C); a comparison of the specimens with bulk Fe_3O_4 is given in Table 2.[35]

The saturation magnetizations achieved are ~66, 68, and 69 emu g^{-1} in EA, IPA, and *n*PA respectively, and the M_S values for the remaining samples were clustered at ~60 emu g^{-1} of sample.

The M_S values obtained are slightly lower than the reported value for bulk magnetite[35] but are sufficient for biomedical applications. This decrease from the bulk value was already reported to be the result of spin canting due to spin frustration and lattice strain in small particles manifested at the surface of the particles, which prevents the co-linear spin arrangement on the A and B sub-lattices of the spinel magnetite (AB_2O_4) structure.[36–38] This effect would become dominant with decreasing particle size.

All the Fe_3O_4 specimens have significant coercivity (H_C, reversed field required to reduce M_R to zero) in the range of 187 to 197 Oe and remnant magnetizations in the range of ~12 to 14 emu g^{-1} (inset of Fig. 4) except the pure magnetite produced in water, which shows a negligible coercive field (3.95 Oe) and M_R value (0.74 emu g^{-1}) as well as a smaller M_S value (57 emu g^{-1}). The reported coercive field for bulk magnetite is 115 to 150 Oe. In general, the enhancement in coercivity and reduction in M_S could be due to an increased magnetite interparticle distance concomitant with a weaker dipolar interaction and other surface effects, which can be pronounced under certain conditions in the nano-regime.[39,40] An alternative explanation for the increase of the coercivity of the NPs produced in alcohols with different polarities is the stronger obstacles when the domains of magnetite attempt to turn under an applied field.[41] When the magnetite NPs are limited and entrenched in the leftover alcohol/glycol, they can be considered as pinned. Since the hysteresis loops of the samples are sensitive to crystal size, they are useful for magnetic grain sizing of natural samples.[42] High H_C in iron oxides is largely governed by magnetocrystallinity, shape, and magnetostrictive (stress-induced) anisotropy along with the polycrystallinity (multi-domain nature) factor, which further depends on the local magnetic anisotropy and the ferromagnetic exchange energy. The ferromagnetic exchange interaction is reported to determine the magnetic behavior of the smaller crystals.[35]

High H_C due to polycrystallinity is ruled out in our study, as the crystallite sizes calculated from the X-ray peak broadening

(Scherrer equation) are equal to or smaller than the physical sizes obtained from the TEM measurements (Table 2). Furthermore, we have already established from the HR-TEM images (Fig. 2) that the NPs synthesized from all the solvents are single crystals. Compared to mono-ol solvent systems, the particles from poly-ol systems are relatively smaller, and as the particle size decreases, the remanance decreases, indicating "single domain" behavior in the MNPs.

The BET adsorption–desorption isotherms for all the specimens showed hysteresis loops of type IV by Brunauer's classification, with an apparent hysteresis loop in the range of 0 to 0.89 P/P_0, indicating the presence of mesopores (data not shown). The pores in the materials are in the mesoporous range (3.6 to 9.5 nm) and are interparticulate in nature. The magnetite products show relatively high surface areas (84 to 183 $m^2\ g^{-1}$), as expected from their small particle sizes. The magnetite synthesized from alcohol mediated precipitation shows a higher surface area (114 to 183 $m^2\ g^{-1}$) compared to the aqueous product (84 $m^2\ g^{-1}$). The size (D_{BET}) estimated from the nitrogen adsorption–desorption isotherms is somewhat larger than the size estimated from TEM (Table 1) for all except the crystals derived from EG, DEG and PEG solvents. Therefore, the particle size and surface area of MNPs can be tuned by changing the dielectric constant of the reaction medium by selecting different alcohols.

The crystalline non-agglomerated dispersible NPs of magnetite obtained by alcohol mediated syntheses are attractive because they are readily dispersible in water using a low energy ultrasonic bath and are able to form transparent colloidal suspensions under ambient conditions. The hydrodynamic size, zeta potential, suspension stability, and optical images of the aqueous suspensions of magnetite nanocrystals (particle concentration 4.3 mM, slightly acidic pH) are illustrated in Fig. 5. The number average size (N_{av}) of 16 to 33 nm of the 40 and 80 °C precipitated powders, with the exception of the water and IPA/water systems, is ~2 to 3 times larger than those of the primary particles as observed by TEM (see Fig. 5A and Table S2†). This is possibly due to tetrahedral or hexagonal close-packed assemblies of ~10 nm particles in the suspension. The N_{av} is reliable as the PDI values are below 0.3, in most cases, which is indicative of narrow and monodisperse size distribution.[43] These aqueous magnetite fluids may find use in various *in vivo* biomedical applications. The colloidal stability of the NPs is closely related to their surface chemistry. The average ζ-values are in the 20.3 to 43 mV range, among which IPA has the least zeta potential and EG has the highest (43 mV) for poly-ol mixed solvent, followed by EA (40.9 mV), which is the highest among the mono-ol solvents (Fig. 5B and Table S2†). The alcohol moieties show slightly acidic behavior when Fe_3O_4 crystals (IEP at pH ~ 6.7) are suspended in them, and the suspension exhibits positive zeta potential due to the positive surface charge over the nanocrystal surfaces. The particle surfaces are positively charged and the strong repulsive forces (electrostatic) among the particles counteract the attractive forces due to magnetic interaction and van der Waals attractive forces and prevent consequent clustering, although the measurements were carried out at their natural pH values (6 to 7) where no electrostatic repulsion is expected. The consequent strong electrostatic repulsive forces can be elucidated by analyzing the energy barrier for aggregation between two approaching particles based on DLVO theory,[7] which can be described as:

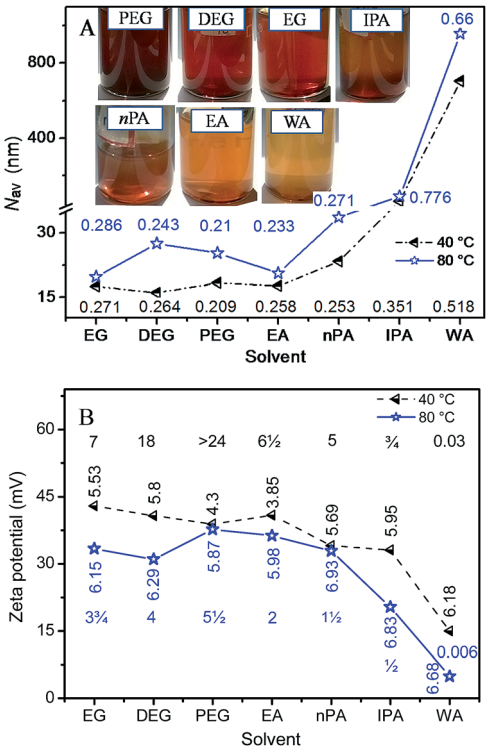

Fig. 5 (A) Hydrodynamic sizes and the corresponding PDI and (B) zeta potential, as well as the stability (horizontal numeric; weeks) of the magnetite suspensions at their natural pH values (vertical numeric), synthesized at 40 and 80 °C in different alcohol–water mixed solvents. Optical images of the freshly prepared dispersions in water are shown as the inset of panel A.

$$V_b = -\frac{A\kappa\alpha}{12} + 2\pi\varepsilon\alpha\psi^2 \quad (4)$$

where α is the particle diameter, ε is the dielectric constant of the solution, and ψ is the surface potential. The effective Hamaker constant A and the Debye–Hückel parameter κ remain constants in our experimental conditions. Therefore, it is evident that the energy barrier V_b largely depends on the dielectric constant of the medium.

It is interesting to note that the products obtained at 40 °C are easily dispersible, and their colloidal stabilities are much higher than those produced at 80 °C (Fig. 5). This is due to the strong positive surface charge as indicated by the high zeta potential at their natural pH values of ~6.4 to 6.9 being close to PZC (see Fig. S7 in the ESI†). The narrow size distribution and the corresponding normalized single exponential decay of the self-correlation coefficient for all MNP clusters produced at 40 °C support their monodisperse nature, especially for the polyol based MNPs (Fig. S4†). The EG, DEG, PEG, EA, and *n*PA dispersions were found to have narrow size distributions, which implies good stability, whereas relatively less stable dispersions

produced broader distributions due to aggregation (in the case of WA and IPA). PEG dispersion (D_{TEM} 10.2 nm) is very stable without any precipitation, even after 6 months of storage. Meanwhile, the IPA slurry, with slightly smaller D_{TEM} size (10.03 nm) and higher CI and PDI as well as the lowest ζ-potential next to water, precipitates completely in 5 days. This suggests that an additional mechanism, *i.e.*, steric effects, in addition to the electrostatic stabilization process (indicated by the ζ-value of ~38 mV) is introduced by the PEG chains.[29] Similar phenomena were observed with EG and DEG; however, the suspensions were stable for 7 and 18 weeks, respectively, due to the poorer stabilizing efficiency of mono and di-ethylene glycol compared to that of PEG, and their Z_{av} sizes are slightly larger (Table S2†). The EA colloids did not sediment over $6\frac{1}{2}$ weeks, probably because of the electrostatic (higher ζ-potential of ~40 mV) and steric effects, and this interaction was supported by FTIR (Fig. S3†). The PCS size along with the correlation fits and zeta potential data of one of the representative specimens (EA) are given in Fig. 6. A Z_{av} size of ~25 nm with a relatively low PDI value of 0.252 is extracted from the good cumulant fit to the auto-correlation function of the intensity fluctuations of scattered photons. The phase plot of this sample is excellent (panel B in Fig. 6).

Magnetite particles with interfacial and even magnetic interactions (due to their small remanence) are also reported to support the clustering process,[44] which contributes to the formation of fractal aggregates[42] with large sediment volumes. With time, when the loose aggregates reach a critical size, the thermal motion cannot hold them in suspension, causing initiation of the sedimentation process. As time elapses, large aggregates drag smaller particles with them and create a significant depletion of nanometer-sized magnetites in the supernatant,[45] forming a color gradient with a clear colorless fluid zone at the top and a gradual increase in color intensity to the bottom. This phenomenon was observed in all the mono- and poly-ol mediated nanocrystal slurries (optical photographs for EG are shown in the inset of Fig. 6B). As expected, the aqueous suspensions of bare MNPs (WA80 and WA) produced in water medium have the least positive surface charges of 4.9 and 15 mV, respectively, with highly polydisperse natures (PDI > 0.5), and do not show any colloidal stability (precipitated within a couple of hours of suspension). $-OH_2^+$ ions exist on the surface of the bare NPs at pH ~ 7 in the vicinity of the isoelectric point of synthetic magnetite, and the suspension is normally not stable.[46] Higher stability of the bare MNP suspension may also be achieved at pH > 10, when ζ almost reaches a plateau in the ζ *versus* pH profile (Fig. S7†).[29] This once again supports the fact that the higher ζ-potential in a nanofluid confers greater colloidal stability. The zero charges on the surface of WA, nPA, PEG and EA magnetite were found to be at pH 6.9, 6.46, 6.47 and 6.4, respectively. Although the natural pH of glycol/alcohol mediated MNPs varies slightly from that of the water mediated NPs, the behaviors of their zeta curves are almost the same as the conditions vary from acidic to basic (Fig. S7†). This leads to the confirmation that the magnetite MNP surface properties are unaltered, irrespective of the synthetic media.

The increase in particle size with increasing dielectric constant of the precipitating solvent is due to enhanced hydrogen bonding. The roles of the increased precipitation temperature and dielectric constant of the solvents are: (1) the crystallinity and particle size of MNPs increase and the colloidal stability in the aqueous phase decreases; (2) the increased precipitation temperature decreases the density of the surface adsorbed alcoholic moieties, resulting in poorer suspension stability.

Glycol medium produced MNPs with narrow size distribution, as observed from D_{TEM}, which may have helped to produce a stable suspension comparable to those in mono-ol media and pure water at 40 °C. The EG dispersion is almost transparent and remains homogeneous, without any visible precipitation or creaming.

Fig. 7 shows the temperature dependent hydrodynamic properties of the PEG based colloid. The hydrodynamic size of 33.3 nm grew to 38.2 nm at 20 to 35 °C, remained almost constant up to 45 °C, and then decreased back to 33.1 nm when the temperature was further increased to 65 °C; however, interestingly, the N_{av} (number average) of ~18 nm remains the same. As expected, the concomitant change in mean count with Z_{av} may be due to the change in the aggregate sizes. The increase in size and mean photon counts up to 45 °C may be due to a slight transformation of the cluster structure from the initial hexagonal shape ($3 \times D_{TEM}$) to one-shell octahedral close-packed ($4 \times D_{TEM}$) and back to hexagonal at ~65 °C. The poly-ol (PEG, DEG and EG) mediated MNC based colloids are stable, do

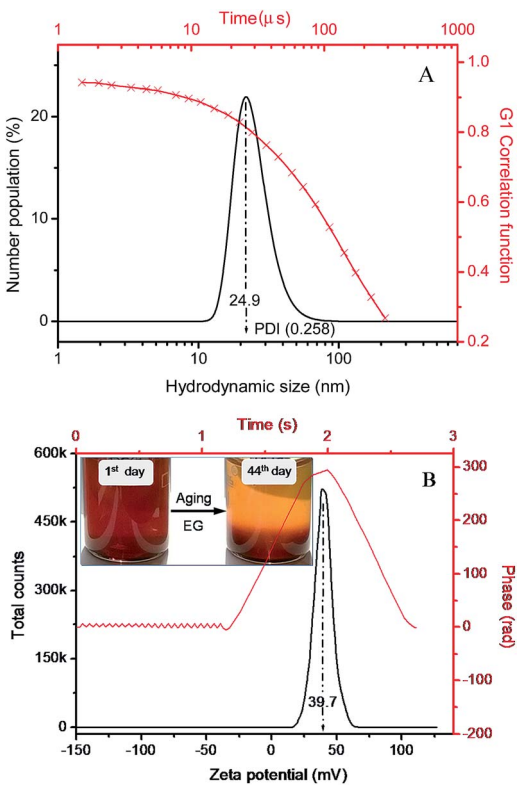

Fig. 6 (A) Hydrodynamic size plot along with the correlation data and (B) zeta potential graph with its phase plot for the EA dispersion in water. The inset is the color gradient formed after incubation of EG for 44 days.

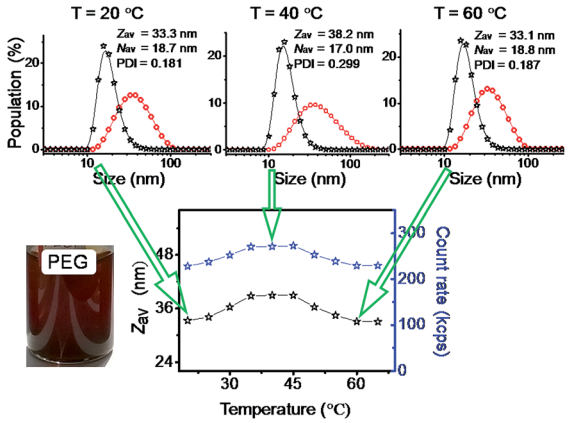

Fig. 7 Temperature dependent PEG agglomerate size in suspension by photon correlation spectroscopic studies. An optical image of the PEG suspension is shown in the inset.

not grow, and precipitate (all data not presented here) over 6–24 weeks as a function of temperature (up to 65 °C). However, these colloids exhibited gradual size growth by 15 to 25% on dilution (up to × 10) due to partial desorption of the chemisorbed poly-ols; hence, they are activated with respect to interaction with other NPs or NPCs.[47]

As anticipated, the DLS data indicated a slight increase in the hydrodynamic size of the particles, with a steadily decreasing count rate for PEG immediately after dilution. A good linear relationship (R^2 = 0.9983) was observed between the count rate and the NPs concentration in the range of 10 to 1.25 mM (Fig. S5†).

The presence of organic layers on the surface of the NPs was further confirmed by TG-DTA. The thermogravimetry patterns of magnetite specimens synthesized from mixed solvents are presented in Fig. 8. All the TG profiles show very similar patterns, with three-step decomposition in the temperature range of 50 to 1000 °C.

The aqueous precipitated magnetite presents a simple two stage thermal decomposition at ~225 and 330 °C consisting of a total loss of ~6%, whereas the total losses are ~11.8, 13.9, and 16.7% for PEG, DEG and EG respectively at temperatures

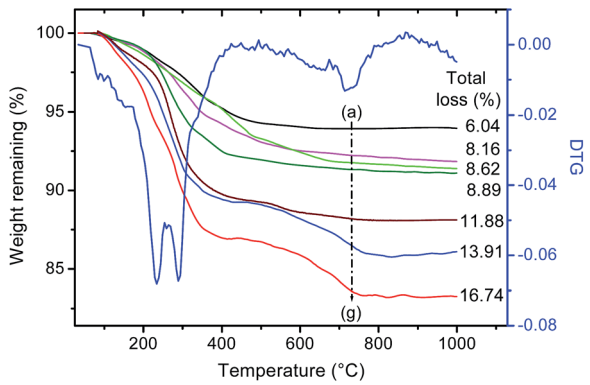

Fig. 8 Thermal analysis patterns of magnetite powders synthesized at 40 °C from a 1 : 1 combination of water with different solvents: (a) WA, (b) *n*PA, (c) EA, (d) IPA, (e) PEG, (f) DEG and (g) EG; DTG of the representative specimen DEG.

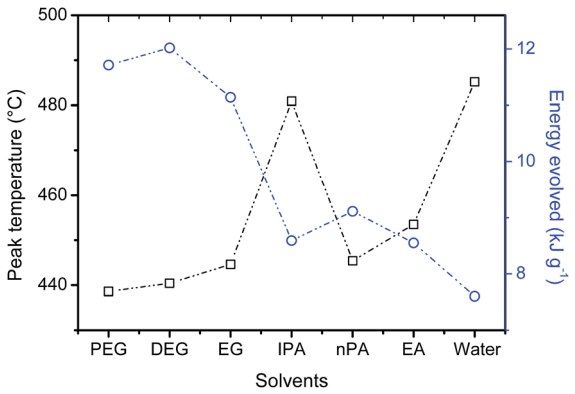

Fig. 9 Differential thermal analysis patterns of magnetite powders synthesized at 40 °C from WA, *n*PA, EA, PEG, DEG, EG, and IPA.

>800 °C. The peak centered at ~120 °C is responsible for the removal of structural water from the lattice, followed by an exothermic peak at ~250 °C for the removal of unwashed salt from the material along with alcohols attached to the surfaces of the nanocrystals. The last peak for a small loss at ~670 °C is due to the combustion of carbon/graphitic products from the decomposition of poly-ols. The weight loss is greater for EG compared to other poly-ols, due to the smaller NPs having higher surface areas available to the adsorbed poly-ol moieties. The TG patterns of *n*PA, EA and IPA have similar losses of ~8.5%.

The catalytic activity of the Fe_3O_4 powders was evaluated by measuring the peak combustion temperature (T_P) and the total heat evolved (ΔH) during the Fe_3O_4 catalyzed combustion of carbonaceous diesel soot in excess O_2; this is shown in Fig. 9. The catalytic activity of magnetite precipitated in solvent mixtures with different dielectric constants is correlated with the BET surface area and active crystal facets. The poly-ol mediated products (PEG, DEG and EG) showed better activity due to their relatively smaller sizes with abundant active (220) and (400) crystal facets. The figure shows that the catalytic activity, in terms of the total heat evolved from the carbon soot combustion, varies from a minimum of 7.6 kJ g^{-1} for WA to a maximum of 12.0 kJ g^{-1} for DEG. The T_P are, as expected, inversely related with the total heat evolved; the extremes are 485.2 and 438.6 °C for WA and PEG, respectively.

The energies evolved during soot burning were relatively lower at ~9 kJ g^{-1} for the mono-ol based products, *e.g.*, IPA, *n*PA and EA, possibly due to the lower T_C values for the active (220) and (400) planes (~1.2 and 1.1, respectively). In comparison to the T_P of WA, the values decreased by 39.8 and 31.7 °C in *n*PA and EA, respectively, whereas the T_P remained almost unchanged at 481 °C in IPA. Thus, we conclude that the activity of a magnetite material is attributable mainly to the energetics of the reaction on the exposed (220) and (400) crystal facets in addition to the available surfaces.

Conclusions

Magnetite nanocrystals have been synthesized *via* homogeneous precipitation in solvents in media with decreasing 'ε'

using 1 : 1 EA, *n*PA, IPA, EG, DEG and PEG with water at 40 and 80 °C. The presence of alcohol/glycol content (by TG-DTA and FTIR) and the precipitation temperature are vital for the control of the agglomeration, suspension stability, size and crystallinity of the magnetite. IPA magnetite is relatively crystalline (CI ~89%), next to water, with the highest magnetization of ~68 emu g^{-1}. The crystals observed from HRTEM have a mixture of multi-faceted polyhedral shapes, all of which contain abundant undercoordinated atoms located on their edges and corners, serving as extra active sites for the chemical reaction. The PEG, DEG and EG powders showed better catalytic activity due to smaller particles with abundant active (220) and (400) crystal facets. Nanofluids with greater aqueous stability were obtained from relatively lower precipitation temperatures at 40 °C. Furthermore, the monodispersed transparent colloidal suspension of PEG showed stability over a period of 6 months. The hydrodynamic diameter was <20 nm with the temperature trend up to 65 °C. These MNPs and stable colloids open up opportunities for improving existing biomedical/industrial applications and designing novel technologies in the future.

Acknowledgements

The authors are grateful to the Director, Central Glass & Ceramic Research Institute, Kolkata for permission and extending facilities to carry out the above work. Dr Dipten Bhattacharya is acknowledged for the magnetization studies. SJI and MJ acknowledge CSIR and UGC for their fellowships. We thank 12 FYP CSIR Network project ESC-0103 for funding the PCS facility. Staff members of the HR-TEM, XRD, and Central Instrumentation Facility are also acknowledged for their assistance in obtaining data.

Notes and references

1 Y. Tian, B. B. Yu, X. Li and K. Li, *J. Mater. Chem.*, 2011, **21**, 2476–2481.
2 S. J. Iyengar, M. Joy, C. K. Ghosh, S. Dey, R. K. Kotnala and S. Ghosh, *RSC Adv.*, 2014, **4**, 64919–64929.
3 C. Guerrero-Sanchez, M. Rasa and U. S. Schubert, *US Pat.*, US2010/0092419 A1, 2010.
4 Y. Li, H. Zhu, H. Gu, H. Dai, Z. Fang, N. J. Weadock, Z. Guo and L. Hu, *J. Mater. Chem. A*, 2013, **1**, 15278–15283.
5 Q. Yan, Z. Zhang, Y. Zhang, A. Umar, Z. Guo, D. O'Hare and Q. Wang, *Eur. J. Inorg. Chem.*, 2015, **2015**, 4182–4191.
6 A. P. Liu, X. Li, L. H. Duan, G. P. Qin and H. H. Guo, *J. Supercond. Novel Magn.*, 2010, **23**, 967–970.
7 L. Gao, W. Li, J. Wang and J. K. Guo, *J. Nanopart. Res.*, 1999, **1**, 349–352.
8 D. Ramimoghadam, S. Bagheri and S. B. A. Hamid, *J. Magn. Magn. Mater.*, 2015, **379**, 74–79.
9 L. Vékás, D. Bica and O. Marinica, *Rom. Rep. Phys.*, 2006, **58**, 257–267.
10 B. Kucuk, N. Ozkan and M. Volkan, *J. Phys. Chem. Solids*, 2013, **74**, 1426–1432.
11 T. Usami, K. Kagawa and M. Kawazoe, *JP Pat.*, JP2007130634-A, 2007.
12 T. P. Rudy, F. R. Goodson and M. E. Dudley, *US Pat.*, US4881994 A, 1989.
13 T. P. Rudy, F. R. Goodson and M. E. Dudley, *US Pat.*, US5688740 A, 1997.
14 R. Amutha, M. Muruganandham, G. J. Lee, V. N. Batalova, G. Mokrousov and J. J. Wu, *Adv. Sci. Lett.*, 2011, **4**, 496–500.
15 H. I. Chen and H. Y. Chang, *Colloids Surf., A*, 2004, **242**, 61–69.
16 X. Wang, Z. Zhao, J. Qu, Z. Wang and J. Qiu, *Cryst. Growth Des.*, 2010, **10**, 2863–2869.
17 S. Hamada and E. Matijević, *J. Colloid Interface Sci.*, 1981, **84**, 274–277.
18 K. C. Remani and S. Ghosh, *Trans. Indian Ceram. Soc.*, 2009, **68**, 185–188.
19 S. Garcia-Jimeno and J. Estelrich, *Colloids Surf., A*, 2013, **420**, 74–81.
20 X. Guo and P. Xiao, *J. Eur. Ceram. Soc.*, 2006, **26**, 3383–3391.
21 T. S. Sreeremya, K. M. Thulasi, A. Krishnan and S. Ghosh, *Ind. Eng. Chem. Res.*, 2012, **51**, 318–326.
22 M. R. Chowdhury, V. Fester, G. Kale and O. Cespedes, *J. Nanopart. Res.*, 2014, **16**, 2412.
23 C. Cheng, F. Xu and H. Gu, *New J. Chem.*, 2011, **35**, 1072–1079.
24 H. Zhang, H. Lim, J. Wei and C. Wong, *Nanosci. Nanotechnol. Lett.*, 2011, **3**, 155–160.
25 J. Zhu, S. Wei, Y. Li, L. Sun, N. Haldolaarachchige, D. P. Young, C. Southworth, A. Khasanov, Z. Luo and Z. Guo, *Macromolecules*, 2011, **44**, 4382–4391.
26 Q. He, T. Yuan, S. Wei, N. Haldolaarachchige, Z. Luo, D. P. Young, A. Khasanov and Z. Guo, *Angew. Chem., Int. Ed.*, 2012, **51**, 8842–8845.
27 Q. He, T. Yuan, X. Yan, Z. Luo, N. Haldolaarachchige, D. P. Young, S. Wei and Z. Guo, *Chem. Commun.*, 2014, **50**, 201–203.
28 M. Erdemoglu and M. Sarikaya, *J. Colloid Interface Sci.*, 2006, **300**, 795–804.
29 A. Masoudi, H. R. M. Hosseini, M. A. Shokrgozar, R. Ahmadi and M. A. Oghabian, *Int. J. Pharm.*, 2012, **433**, 129–141.
30 K. Helttunen, A. Galán, P. Ballester, J. Bergenholtz and M. Nissinen, *J. Colloid Interface Sci.*, 2016, **464**, 59–65.
31 J. Baumgartner, A. Dey, P. H. H. Bomans, C. Le Coadou, P. Fratzl, N. A. J. M. Sommerdijk and D. Faivre, *Nat. Mater.*, 2013, **12**, 310–314.
32 C. Liang, S. Huang, W. Zhao, W. Liu, J. Chen, H. Liu and Y. Tong, *New J. Chem.*, 2015, **39**, 2651–2656.
33 B. S. Furniss, A. J. Hannaford, V. Rogers, P. W. G. Smith and A. R. Tatchell, *Vogel's Textbook of practical organic chemistry*, English Publisher Book Society, Longman, England, 4th edn, 1978.
34 http://pharmlabs.unc.edu/labs/solubility/structure.htm, accessed on 10/7/15.
35 M. I. Dar and S. A. Shivashankar, *RSC Adv.*, 2014, **4**, 4105–4113.
36 *The iron oxides: structure, properties, reactions, occurrences and uses*, ed. R. M. Cornell and U. Schwertmann, Wiley-VCH, Wein-heim, 2nd edn, 1996, p. 117.
37 J. M. D. Coey, *Phys. Rev. Lett.*, 1971, **27**, 1140–1142.

38 F. Bødker, S. Mørup and S. Linderoth, *Phys. Rev. Lett.*, 1994, **72**, 282–285.
39 Z. Guo, H. T. Hahn, H. Lin, A. B. Karki and D. P. Young, *J. Appl. Phys.*, 2008, **104**, 014314.
40 Z. Guo, S. Park, H. T. Hahn, S. Wei, M. Moldovan, A. B. Karki and D. P. Young, *Appl. Phys. Lett.*, 2007, **90**, 053111.
41 M. Wu, Y. Xiong, Z. Peng, N. Jiang, H. Qi and Q. Chen, *Mater. Res. Bull.*, 2004, **39**, 1875–1880.
42 S. Ghosh, Ph.D. thesis, Dublin City University, Ireland, 2006.
43 S. J. Iyengar, M. Joy, T. Maity, J. Chakraborty, R. K. Kotnala and S. Ghosh, *RSC Adv.*, 2016, **6**, 14393–14402.
44 M. R. Gittings and D. A. Saville, *Colloids Surf., A*, 1998, **141**, 111–117.
45 J. L. Viota, F. Gonzalez-Caballero, J. D. G. Duran and A. V. Delgado, *J. Colloid Interface Sci.*, 2007, **309**, 135–139.
46 M. Mahmoudi, S. Laurent, M. A. Shokrgozar and M. Hosseinkhani, *ACS Nano*, 2011, **5**, 7263–7276.
47 J. K. Stolarczyk, S. Ghosh and D. F. Brougham, *Angew. Chem., Int. Ed.*, 2009, **48**, 175–178.